Tunable Wave-Propagation Band gap via Stretching Kirigami Sheets

Hesameddin Khosravi* and Suyi Li
Department of Mechanical Engineering, Clemson University, Clemson, South Carolina, USA

(Received 16 November 2021; revised 9 March 2022; accepted 24 May 2022; published 28 June 2022)

This study examines Bragg's band gap and its mechanical tuning in a stretch-buckled kirigami sheet with "zig-zag" distributed parallel cuts. When stretched beyond a critical threshold, the kirigami buckles out of plane and generates a three-dimensional periodic architecture. Our theoretical calculation, numerical simulation, and experiments confirm the transverse elastic wave-propagation band gaps and their correlation to stretching. This result opens an avenue of using kirigami as a simple and effective approach for creating and adapting periodicity for wave-propagation control.

DOI: 10.1103/PhysRevApplied.17.064054

The emergence of mechanical metamaterials, which derive their properties primarily from their underlying architecture, has unleashed an era of material functionality. Exploiting such architecture-property correlations has enabled many desirable and even "unnatural" responses [1–4]. One of the most consequential examples is Bragg's band gap—a phenomenon that the interferences from a periodic array of scatterers can completely stop the propagation of incident waves when their wavelengths are similar to the scatterer's spacing [5]. The ability to manipulate wave propagation via Bragg's band gap has enabled countless applications in noise mitigation [6], wave transmission control [7], acoustic cloaking [8], nonreciprocity [9], and even wave-based mechanical computation [10]. Nonetheless, the potentials of these applications all hinge upon our capability to *fabricate* and *control* periodic architectures in metamaterials. To this end, we have seen a variety of fabrication approaches like three-dimensional (3D) printing [11–13], self-assembly [14], and laser cutting [15]. For controlling (or changing) the periodicity, mechanical deformation [16–18] and lattice reconfiguration [19] have been examined. However, these methods of creating and changing periodicity are two separate processes, which could be time consuming and cumbersome.

In this letter, we show that simply stretching an elastic kirigami sheet is an integrated process to *simultaneously* create and control periodic architectures, providing tunable propagation band gaps for elastic waves at low frequencies. Kirigami is an ancient art of cutting and shaping papers into decorative 3D shapes. It has recently transformed into a design and fabrication framework to engineer flexible electronics [20], superstretchable materials [21], light-weight structures [22], and soft robots [23,24]. Compared to other methods of constructing periodic 3D motifs, the kirigami-inspired approach has many unique advantages. For example, the seemingly infinite possibilities in cutting pattern geometry offer significant freedoms in design [25]. And cutting as a fabrication method is easily scalable from nano- [26], micro- [27], millimeter [28], to meter scale [29].

This study also presents efforts to examine the dynamic responses in kirigami-based material systems. Static properties induced by cutting like stretchability [30–32], auxetics [33], buckling [34,35], and multistability [36,37] have been extensively examined. However, dynamic characteristics in kirigami, such as vibrations and wave propagation, remain largely unexplored.

Here, we focus on the transverse elastic wave propagation in a stretch-buckled kirigami sheet with a "zig-zag" uniform distribution of parallel slit cuts shown in Fig. 1. A few design parameters—including the cut sizes l_a, l_b, l_c, and the spacing between cuts w—can fully define the overall cutting pattern. When sufficiently stretched in plane along the periodicity direction (the x direction), the kirigami sheet would buckle and develop out-of-plane deformations, creating a linear array of identical unit cells, each consisting of a few curved ligaments. Moreover, controlling the in-plane stretching can directly change the 3D geometry of these unit cells, offering a simple approach for turning the dynamic responses. The stretch-buckled kirigami sheet's overall height and width are significantly smaller than its length, and we assume that its shearing deformation and rotational inertia are negligible by ensuring small transverse elastic wave magnitude. So the Euler-Bernoulli beam condition applies, and the governing equation for the wave propagating along the longitudinal x direction is

$$\frac{\partial^2}{\partial x^2}\left[EI(x)\frac{\partial^2 U(x,t)}{\partial x^2}\right]+\rho A(x)\frac{\partial^2 U(x,t)}{\partial t^2}=0. \quad (1)$$

*hkhosra@clemson.edu

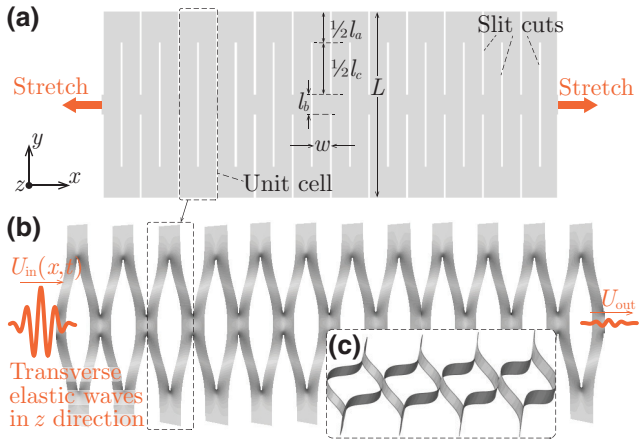

FIG. 1. The overall concept of this study. (a) A kirigami sheet with "zig-zag" patterned parallel cuts, whose geometry can be defined by just a few parameters. Here, we neglect the slit cuts' width. (b) The external shape of a stretched-buckled kirigami sheet, simulated in ABAQUS (3D solid elements with explicit solver). It exhibits a controllable, 3D periodic architecture, generating Bragg's band gaps for out-of-plane transverse elastic waves. (c) A different view of the kirigami highlighting the curved ligaments.

Here, ρ and E are the mass density and Young's modulus of the constitutive sheet material, respectively; $U(x,t)$ is the out-of-plane transverse displacement in the z direction; and $A(x)$ and $I(x)$ are the distributions of the cross-section area and the area moment of inertia in the buckled kirigami sheet, respectively. It is worth noting that this governing equation of motion does not involve stretch force. At moderate stretch (postbuckling), the kirigami deforms out of plane and shows almost constant reaction force [34,35]. Therefore, the result of stretching is mostly shape change in $A(x)$ and $I(x)$ rather than generating more internal stress.

Calculating $A(x)$ and $I(x)$ is quite challenging because of the buckled kirigami sheet's complicated 3D geometry, especially the curved ligaments. Therefore, we introduce "virtual folds" at critical locations on the ligaments that exhibit the most concentrated bending deformation and assume that the facets in-between these folds are flat surfaces (surfaces A, B, and C in Fig. 2). Indeed, these folds can naturally occur when the stretching is strong enough to induce plastic deformation [34], so they could represent the mechanics of buckled kirigami sheets with reasonable accuracy. Moreover, the simplified kirigami becomes rigid foldable, making the kirigami deformation a one-degree-of-freedom mechanism.

Figure 2(d) elucidates the complex $A(x)$ and $I(x)$ distributions in a unit cell subject to different amounts of in-plane stretch. Here, we use the dihedral angle φ between surface B and the y-z reference plane to describe stretching; the detailed calculations are available in the Appendix A.

Denote $\mathbf{R} = a_1\mathbf{e}_1$ as a translational vector in *direct space*, representing the periodicity [Fig. 2(b)]. That is, we can construct the kirigami sheet by a set of infinite translational operations of the unit cell based on $\mathbf{R}$. In this case, a_1 is an integer number, and the lattice vector $\mathbf{e}_1$ lies in the x direction. We then define the reciprocal lattice vector $\mathbf{G}$ in that $e^{-i\mathbf{G}\cdot\mathbf{R}} = 1$. Here, m_1 is another integer, $\mathbf{G} = m_1\mathbf{b}_1$, and $\mathbf{b}_1$ is the lattice vector in *reciprocal space*. Equivalent to the lattice vector $\mathbf{e}_1$ in direct space, infinite translation operations of the reciprocal lattice vectors $\mathbf{b}_1$ define *reciprocal space*, which has similar symmetry to direct space. Like in the direct lattice, an equivalent unit cell can then be defined in reciprocal space based on $\mathbf{b}_1$, giving us the first Brillouin zone (FBZ).

To analyze the wave-propagation behavior in the stretch-buckled kirigami sheet, we employ the plane-wave expansion (PWE) method. First, a separation of variables gives $U(x,t) = \tilde{U}(x)e^{-i\omega t}$, where ω is the harmonic oscillation frequency. Based on the Blotch theorem, we can formulate the spatial term $\tilde{U}(x)$ for the whole kirigami sheet into a product of plane-wave and periodic functions in the first irreducible Brillouin zone so that

$$\tilde{U}(x) = e^{i(2\pi k_1 x)} \sum_{n_1} \hat{U}(n_1) e^{i(2\pi n_1 x)}, \tag{2}$$

where n_1 is an integer and k_1 is a wave number within the FBZ in that $k_1 \in [0, \frac{1}{2}]$. We further expand the distribution of cross-section area $A(x)$ and area moment of inertia $I(x)$ in Fourier series so that

$$A(x) = \sum_{m_1} \hat{A}(m_1) e^{i(2\pi m_1 x)}, \tag{3}$$

$$I(x) = \sum_{m_1} \hat{I}(m_1) e^{i(2\pi m_1 x)}. \tag{4}$$

By substituting the formulations above into the governing equation, Eq. (1), and denoting by b_1 the magnitude of the reciprocal lattice vector ($b_1 = |\mathbf{b}_1|$), we obtain the eigenvalue problem for calculating the dispersion curves. More details are given in the Appendix B, and a few results are highlighted in Fig. 3(a). We have

$$\sum_{n_1} \left[E(n_1 + k_1)^2 (k_1 + m_1 + n_1)^2 \hat{I}(m_1) - \omega^2 \left(\frac{\rho}{b_1^4} \right) \hat{A}(m_1) \right] = 0. \tag{5}$$

To validate the theoretical prediction of band-gap frequencies, we compare its results to numerical simulations and experimental measurements based on a nylon-based kirigami sample ($E = 9.2$ GPa, $\rho = 1200$ Kg/m^3, material thickness $t = 0.002$ m, with cut sizes $l_a = 0.04$ m, $l_b = 0.02$ m, $l_c = 0.064$ m, and cut spacing $w = 0.01$ m). Regarding the numerical analysis, we first

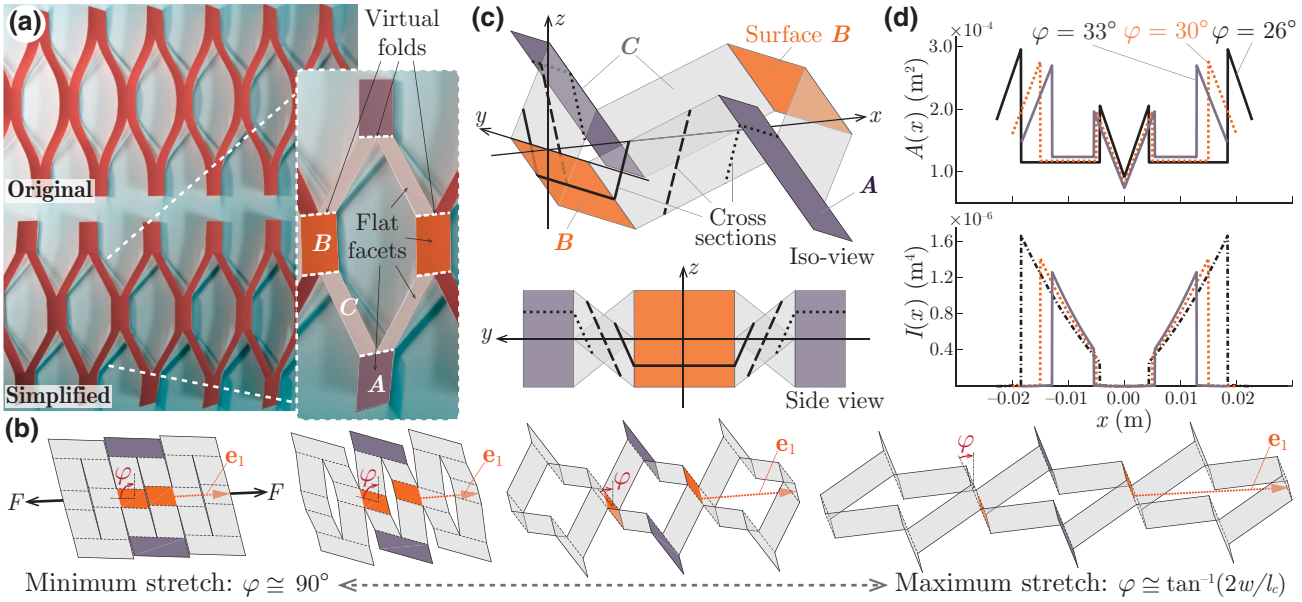

FIG. 2. Simplification and modeling the geometry of a stretch-buckled krigami sheet. (a) Comparing the original and simplified geometry of kirigami sheets; the insert details the "virtual folds" and the flat facets (aka. surfaces A, B, C) between them. (b) Stretching deformations of the simplified kirigami sheet, which shows rigid foldability, and its facets remain flat and undeformed during stretching. The lattice vector $\mathbf{e}_1$ is highlighted. Here, the dihedral angle φ describes the kirigami stretching, and $\varphi = \sin^{-1}(2w/a)$, where a is the unit cell's length after stretch and w is the spacing between cuts. (c) Detailed geometry of a unit cell. The solid and dashed lines highlight the shape of its cross sections. (d) The $A(x)$ and $I(x)$ distributions in a unit cell with different stretches ($l_a = 0.04$ m, $l_b = 0.02$ m, $l_c = 0.064$ m, $w = 0.01$ m, $t = 0.002$ m). Detailed geometric derivations are given in Appendix A.

create a CAD model of the stretch-buckled kirigami sheet in SolidWorks®—based on the simplified geometry in Fig. 2—and export it to COMSOL® software (3D mesh elements and frequency analysis solver; see Fig. 6 within the Appendix C). After the mesh convergence study, we use two reference lines parallel to the y direction at both ends of the kirigami sheet to measure the vibration entering and exiting structure at specific ranges of frequencies. Then, the wave transmissibility is defined as $\mathrm{TR} = \tilde{U}_{\mathrm{out}}/\tilde{U}_{\mathrm{in}}$, where $\tilde{U}_{\mathrm{in}}$ and $\tilde{U}_{\mathrm{out}}$ are the maximum displacement of incoming and transmitted waves, respectively. This transmissibility has been widely used to evaluate the band-gap frequency [38].

Figure 3(b) details the experimental setup. We attach one end of the kirigami sheet to a shaker (Labworks DB-140 with Pa-141 amplifier) to provide the out-of-plane (z-direction) excitation. The other end is attached to a rigid end fixture via thin tape. We carefully choose the tape width w_t to mimic the free boundary condition the best. This tape needs to be wide at low excitation frequency due to a large vibration amplitude but narrow at high frequency; we find that $\tan^{-1}(w_t/\tilde{U}_{\mathrm{out}}) < 6^\circ$ is a good guideline. To measure the wave transmissibility through the stretch-buckled kirigami sheet, we use a signal generator (Tektronix AFG3022c) to generate harmonic excitations with sweeping frequencies and use two laser vibrometers (Polytec OFC-5000) to measure the input and transmitted waves (see Fig. 7 within the Appendix D.

The analytical theory's predictions, COMSOL simulations, and experimental results all confirm the occurrence of Bragg's band gap in the stretch buckled kirigami sheet [Fig. 3(c)]. Moreover, the band-gap frequency can be effectively tuned by simply increasing or decreasing the in-plane stretch. Based on the theoretical prediction, the kirigami sample provides a Bragg band gap between 423 and 681 Hz with a moderate stretch [$\varphi = \sin^{-1}(2w/a) = 33^\circ$, or the kirigami sheet stretched to 183% of its original length]. Stretching the kirigami sheet to 200% of its original length ($\varphi = 30^\circ$) places the band gap to between 465 and 773 Hz. As the kirigami sheet is stretched further to 228% of its original length ($\varphi = 26^\circ$), the band gap moves to between 550 and 838 Hz. Such correlation between stretching and band-gap frequencies is confirmed by numerical simulation and experiment.

While the different test results show good agreement regarding the band-gap frequencies, there are notable differences between the numerical simulation and experiment regarding the magnitude of wave transmissibility. Such discrepancy might come from a combination of different factors, such as fabrication imperfection, the differences between the original and simplified kirigami geometry, and material damping (while the nylon material has significant internal damping, the numerical simulation

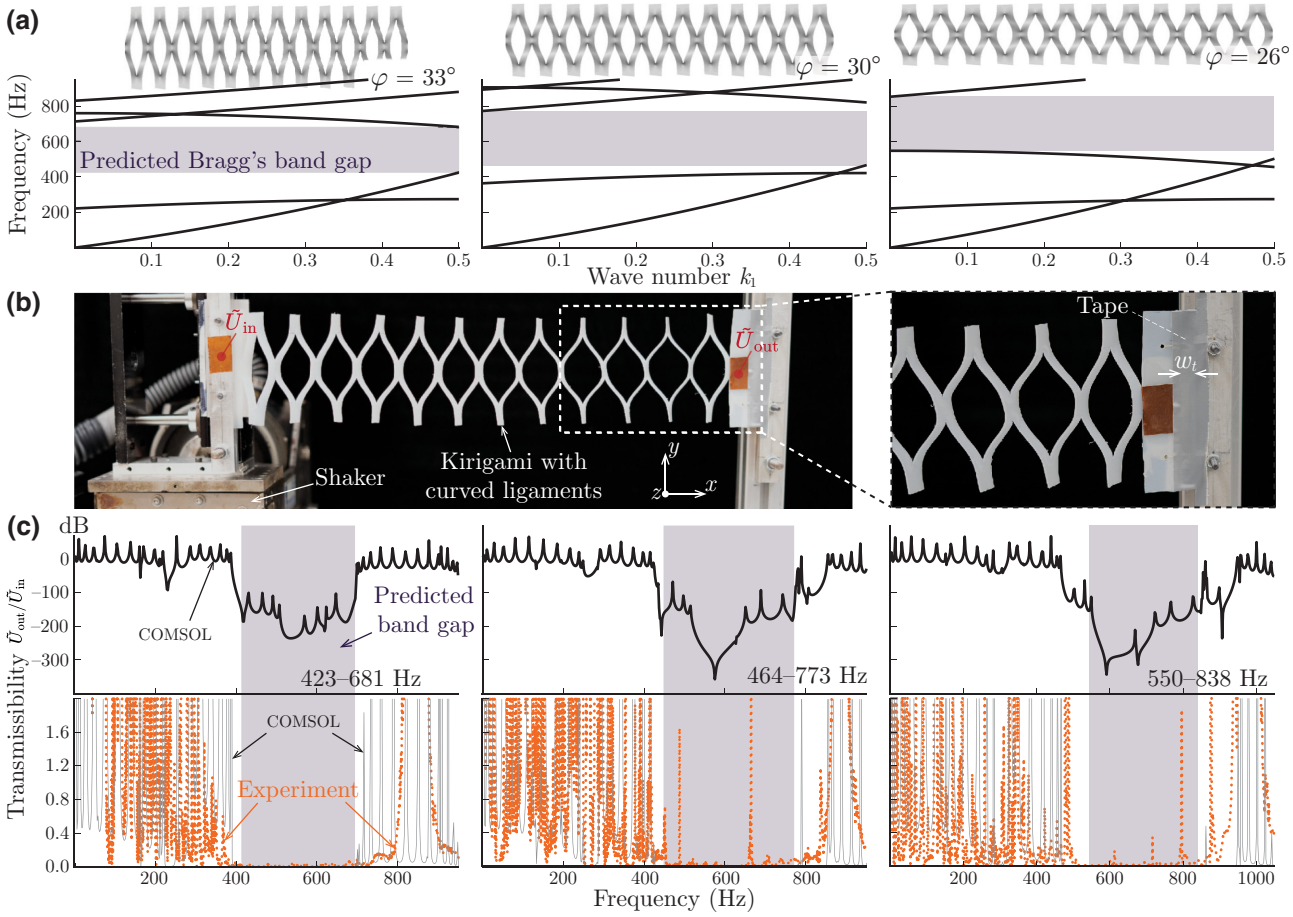

FIG. 3. Summary of simulation and experiment results. (a) Theoretically predicted dispersion relationships at three different levels of stretch, highlighting the first Bragg band gap. (b) The experimental setup (for more details, see Sec. 3 of the Appendix D). (c) First row: the simulated transmissibility *in decibels*; second row: comparison between the same simulation results and experimental measurements *in linear scale*. The experimental results are slightly postprocessed only to eliminate electronic noises.

assumes zero damping to avoid unnecessary computational complexities). Moreover, the analytical model assumes an infinite number of unit cells, while the kirigami experimental sample only has 12. The omission of the tension force in the governing equation is another probable cause for the more considerable discrepancies at the highest tested stretch. Regardless, these results firmly validate our assumptions that stretching elastic kirigami sheets is a simple and effective approach for generating and controlling periodicity in a metamaterial system for wave-propagation control. Moreover, the results elucidate the physical principles underpinning the correlation between stretching and band-gap frequency tuning.

It is worth pointing out that our analytical calculation and COMSOL simulation use the simplified kirigami geometry with virtual folds and flat facets, but the experiments do not. That is, the physical kirigami prototype has curved ligaments. Therefore, the agreement between these results indicates that the kirigami geometry simplification summarized in Fig. 2 provides an reasonably accurate correlation between the Bragg band gap and kirigami design and stretching. Therefore, our theory can serve as a quick and effective design tool for kirigami-based metamaterial systems, and it could be expanded to more complicated cut patterns.

Finally, the simplicity and versatility in kirigami cutting pattern design offer us significant freedom to prescribe and control the wave-propagation band gaps. We apply our theoretical method to three kirigami sheets and examine their band-gap frequencies at different stretch levels (Fig. 4). These sheets share the same constitutive material, overall size, and cut spacing. The only difference between them is the cut lengths, which are very simple to change during fabrication. Yet, the three kirigami sheets exhibit significantly different and tunable band-gap frequencies.

In conclusion, we use theoretical, numerical, and experimental methods to examine Bragg's elastic wave-propagation band gaps in stretch-buckled kirigami sheets. Our results show that we can prescribe and tune the band-gap frequencies with considerable freedom by simply

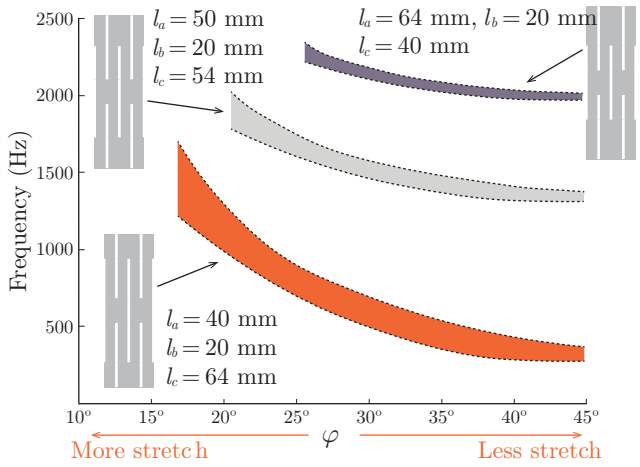

FIG. 4. The Bragg band-gap frequencies are directly related to the kirigami cutting pattern design and in-plane stretching. Note that the φ values correspond to the maximum stretch and vary for different cut pattern designs.

tailoring the cutting pattern and controlling the in-plane stretch. The results of this study open an avenue for using kirigami-based metamaterial systems with adaptive periodicity for wave-propagation control.

ACKNOWLEDGMENTS

The authors acknowledge support from Clemson University (via a startup fund and CECAS Dean's Faculty Fellow Award) and the National Science Foundation (CMMI-1760943).

APPENDIX A: SIMPLIFYING KIRIGAMI'S GEOMETRY

Figure 1(a) in the main text explains the parameters defining the parallel and zig-zag distributed cutting pattern. Here, l_a, l_b, and l_c define the slit cuts' size; w is the spacing between two cuts along the longitudinal direction. Once buckled via stretching, the kirigami sheet takes a complicated three-dimensional shape with significant out-of-plane deformation. As a result, the buckled kirigami structure has a finite thickness, satisfying Euler-Bernoulli's beam geometrical conditions. In other words, the stretch-buckled kirigami sheet becomes a beamlike structure consisting of a linear periodic array of "unit cells," as shown in Figs. 1(b) and 1(c).

The ligaments inside the unit cells exhibit complex deformations with a nonuniform curvature distribution, making it challenging to calculate the parameters relevant to wave-propagation analyses, such as the cross-sectional area and area moment of inertia. To address this challenge, we introduce "virtual folds" at critical locations on the ligaments that exhibit the most concentrated bending deformation and assume that the facets in-between these folds are flat surfaces (surfaces A, B, and C in Fig. 2 of the main text). The simplified kirigami becomes rigid foldable, making the kirigami deformation a one-degree-of-freedom mechanism.

To solve the dynamic equation of motion for wave propagation, we need to calculate the distributions of the cross-sectional area $A(x)$ and area moment of inertia $I(x)$ over a unit cell, where x represents the longitudinal direction. To this end, we choose the dihedral angle (φ) between surface B within the kirigami unit cell and the y-z reference plane as the independent variable [Figs. 2(b) and 5]. When the kirigami sheet is undeformed (or flat in the x-y reference plane), φ takes the maximum value ($\varphi_{\max} = \pi/2$); when the buckled kirigami sheet is fully stretched, φ takes the minimum value:

$$\varphi_{\min} = \tan^{-1}\left(\frac{2w}{l_c}\right). \tag{A1}$$

We also denote the dihedral angle between surface C defined in Fig. 2 and the x-z reference place as β, so that

$$\beta = \cos^{-1}\left(\frac{2w}{l_c \tan\varphi}\right). \tag{A2}$$

When the kirigami sheet is undeformed (flat), $\beta = \pi/2$; when the kirigami sheet is fully stretched, $\beta = 0$. The overall length of the unit cell is

$$a = \frac{2w}{\sin\varphi}. \tag{A3}$$

Another important geometric variable is the *projected* length of surface C along the y axis, as illustrated in Fig. 5(b):

$$d = w\frac{\tan\beta}{\tan\varphi} = \sqrt{\frac{l_c^2}{4} - \frac{w^2}{\tan^2\varphi}} = \frac{l_c}{2}\sin\beta. \tag{A4}$$

Here, we assume that the kirigami sheet is highly stretched after buckling in that $\phi_{\min} < \varphi < \pi/4$ (assuming that $l_c > 2w$). We can divide half of the unit cell in this case into three sections [sections i, ii, and iii in Fig. 5(c)] because the cross sections take distinct shapes in these three sections.

Section i corresponds to $0 < x < w\sin\varphi$, and the cross-sectional area involves surface B and surface C. The cross section [solid lines in Fig. 5(b_i)] is the summation of these two parts so that

$$\begin{aligned} A_i(x) &= \frac{t}{\sin\varphi}(l_b + 2L_i^C) \\ &= \frac{t}{\sin\varphi}\left(l_b + \frac{x}{w\sin\varphi}\sqrt{4w^2 + l_c^2\tan^4\varphi}\right), \end{aligned} \tag{A5}$$

where t is the thickness of the kirigami sheet material. The area moment of inertia with respect to the y axis also

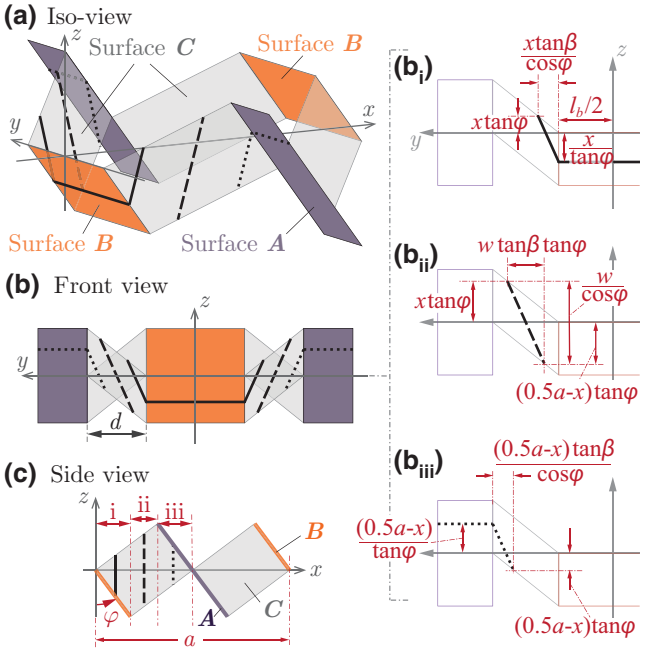

FIG. 5. The unit-cell geometry of a simplified kirigami sheet with a relatively large stretch. (a)–(c) The isometric, front, and side views of the kirigami unit cell, respectively. The independent variable φ and the three sections in the half unit cells are highlighted in the side view. (b_i)–(b_{iii}) Close-up front views of the cross-section area corresponding to different ranges of x values. Note that the solid, dashed, dotted black lines are the cross sections of the kirigami unit cell in three different sections.

includes two parts:

$$I_i(x) = I^B + l_b\frac{t}{\sin\varphi}\left(\frac{x}{\tan\varphi}\right)^2 + 2I_i^C + 2\frac{x\tan\beta}{\cos\varphi}\frac{t}{\sin\varphi}\left(\frac{x\tan\varphi - x\cot\varphi}{2}\right)^2. \quad \text{(A6)}$$

Here the first two terms come from the cross section of surface B (using the parallel axis theorem), and the third and fourth terms come from the cross section of surface C. Here, I^B is the bending moment of inertia of surface B's cross section with respect to its own neutral axis in that

$$I^B = \frac{l_b}{12}\left(\frac{t}{\sin\varphi}\right)^3. \quad \text{(A7)}$$

Similarly, I_i^C is surface C's area moment of inertia with respect to its own neutral axis in that

$$I_i^C(x) = \frac{t}{12\sin\varphi}\frac{x\tan\beta}{\cos\varphi}\left[\frac{t^2}{\sin^2\varphi} + x^2(\tan\varphi + \cot\varphi)^2\right]. \quad \text{(A8)}$$

Section ii corresponds to $w\sin < x < a/2 - w\sin\varphi$, and the overall cross-section area involves surface C [dashed line in Fig. 5(b_{ii})]:

$$A_{ii}(x) = 2\frac{t}{\sin\varphi}L_{ii}^C = \frac{t}{\sin\varphi}\sqrt{4w^2 + l_c^2\tan^4\varphi}. \quad \text{(A9)}$$

The area moment of inertia with respect to the y axis is

$$I_{ii}(x) = 2I_{ii}^C + 2\frac{t}{\sin\varphi}[(a/4 - x)\tan\varphi]^2, \quad \text{(A10)}$$

where

$$I_{ii}^C = \frac{t}{12\sin\varphi}w\tan\varphi\tan\beta\left(\frac{t^2}{\sin^2\varphi} + \frac{w^2}{\cos^2\varphi}\right). \quad \text{(A11)}$$

Finally, section iii of the half unit cell corresponds to $\sin\varphi < x < a/2$. In this section, the cross section [dotted line in Fig. 5(b_{iii})] involves surfaces A and C in that

$$A_{iii}(x) = \frac{t}{\sin\varphi}(l_a + 2L_{iii}^C) = \frac{t}{\sin\varphi}\left(l_a + \frac{a/2 - x}{w\sin\varphi}\sqrt{4w^2 + l_c^2\tan^4\varphi}\right). \quad \text{(A12)}$$

The corresponding area moment of inertia with respect to the y axis includes two components in that

$$I_{iii}(x) = I^A + l_a\frac{t}{\sin\varphi}\left(\frac{a/2 - x}{\tan\varphi}\right)^2 + 2I_{iii}^C + 2\frac{(a/2 - x)\tan\beta}{\cos\varphi}\frac{t}{\sin\varphi} \times \left[\frac{(a/2 - x)(\tan\varphi - \cot\varphi)}{2}\right]^2, \quad \text{(A13)}$$

where

$$I_{iii}^C(x) = \frac{t}{12\sin\varphi}\frac{(a/2 - x)\tan\beta}{\cos\varphi} \times \left[\frac{t^2}{\sin^2\varphi} + (a/2 - x)^2(\tan\varphi + \cot\varphi)^2\right] \quad \text{(A14)}$$

and I^A is the bending moment of inertia of the cross-section area in surface A with respect to its own neutral axis so that

$$I^A = \frac{l_a}{12}\left(\frac{t}{\sin\varphi}\right)^3. \quad \text{(A15)}$$

The final results of $A(x)$ and $I(x)$ corresponding to different amounts of stretch are summarized in Fig. 2(d).

APPENDIX B: SOLVING THE BAND GAPS USING THE PWE METHOD

To obtain the band structure of the stretch-buckled kirigami sheet, we apply Bloch's theorem to its unit cells in the reciprocal lattice space (aka. Brillouin zone). It is worth noting that the formulations in this section apply to generic two-dimensional periodic structures, and we highlight the simplification for a 1D periodic stretch-buckled kirigami sheet at the end.

First, we review the fundamental concepts describing the geometry of periodic structures. A generic two-dimensional periodic structure can be constructed by an infinite set of translation operations on its unit cell along with specific directions. Such operations can be represented by translational vectors $\mathbf{r}$:

$$\mathbf{r} = a_1\mathbf{e}_1 + a_2\mathbf{e}_2. \tag{B1}$$

Here $\mathbf{e}_1$, $\mathbf{e}_2$ are the lattice vectors in *direct space*, and a_1, a_2 are integers. The dimension of this translational vector depends on the nature of the underlying periodicity. The stretch-buckled kirigami sheet in this study is periodic only in the x direction, so $\mathbf{r}$ is one dimensional and $\mathbf{r} = a_1\mathbf{e}_1$, where $\mathbf{e}_1$ aligns with the x direction.

The reciprocal lattice is described by a set of vectors $\mathbf{G}$ that satisfy the relationship

$$e^{-i\mathbf{G}\cdot\mathbf{r}} = 1, \tag{B2}$$

where $\mathbf{G} = m_1\mathbf{b}_1 + m_2\mathbf{b}_2$. Here, $\mathbf{b}_1$ and $\mathbf{b}_2$ are the lattice vectors in *reciprocal space*; m_1, m_2 are integers. Equation (B2) indicates that the reciprocal lattice vectors $\mathbf{b}_1$, $\mathbf{b}_2$ are orthogonal to the lattice vectors $\mathbf{e}_1$, $\mathbf{e}_2$ in that

$$\mathbf{e}_i \cdot \mathbf{b}_j = 2\pi\delta_{ij}. \tag{B3}$$

Just like the lattice vectors $\mathbf{e}_1$, $\mathbf{e}_2$ that can define periodicity in direct space, infinite translations of the reciprocal lattice vectors $\mathbf{b}_1$, $\mathbf{b}_2$ define reciprocal space, which has similar symmetry properties to that of direct space. In a stretch-buckled kirigami sheet, the lattice vector $\mathbf{r} = a_1\mathbf{e}_1$ aligns with the x direction, so the reciprocal lattice vector is $\mathbf{G} = m_1\mathbf{b}_1$, also in the x direction. More importantly, $\mathbf{b}_1$, $\mathbf{b}_2$ define the elementary unit cell in reciprocal space, which is called the first Brillouin zone. The importance of this Brillouin zone stems from the Bloch wave description of the wave field in periodic media: Bloch wave descriptions in the first Brillouin zone can fully characterize the solutions.

Next, we turn to the application of the PWE method for solving wave equation (1) in the main text and calculating the band-gap structure. Assume that the constitutive material properties E and ρ are constant. The first step in implementing the PWE method is to expand the periodically varying entities—cross-sectional area $A(\mathbf{x})$ and area moment of inertia $I(\mathbf{x})$—into Fourier series.

For a generic, two dimensional periodic system, such expansions take the form

$$A(\mathbf{x}) = \sum_{\mathbf{G}} \hat{A}(\mathbf{G})e^{i\mathbf{G}\cdot\mathbf{x}}, \tag{B4}$$

$$I(\mathbf{x}) = \sum_{\mathbf{G}} \hat{I}(\mathbf{G})e^{i\mathbf{G}\cdot\mathbf{x}}. \tag{B5}$$

In the equations above, the Fourier coefficients $\hat{A}(\mathbf{G})$ and $\hat{I}(\mathbf{G})$ over the unit cell with area $A_{\text{u.c.}}$ can be calculated as

$$\hat{A}(\mathbf{G}) = \frac{1}{A_{\text{u.c.}}} \iint_{A_{\text{u.c.}}} A(\mathbf{x})e^{-i\mathbf{G}\cdot\mathbf{x}}d\mathbf{x}, \tag{B6}$$

$$\hat{I}(\mathbf{G}) = \frac{1}{A_{\text{u.c.}}} \iint_{A_{\text{u.c.}}} I(\mathbf{x})e^{-i\mathbf{G}\cdot\mathbf{x}}d\mathbf{x}. \tag{B7}$$

The next step in the PWE method is to convert the governing dynamic equations of motion into an eigenvalue problem. For a generic 2D periodic structure, we start by applying the separation of variables to the displacement field:

$$U(\mathbf{x}, t) = \tilde{U}(\mathbf{x})e^{-i\omega t} \tag{B8}$$

with ω the harmonic oscillation frequency. We then expand the displacement $\tilde{U}(\mathbf{x})$ based on the Bloch theorem:

$$\tilde{U}(\mathbf{x}) = e^{i\mathbf{K}\cdot\mathbf{x}} \sum_{\mathbf{H}} \hat{U}(\mathbf{H})e^{i\mathbf{H}\cdot\mathbf{x}}. \tag{B9}$$

Here $\mathbf{H} = n_1\mathbf{b}_1 + n_2\mathbf{b}_2$ is a direction vector with integer valued n_1, n_2 and $\mathbf{K} = k_1\mathbf{b}_1 + k_2\mathbf{b}_2$ is the wave vector, whose components are restricted to vary within the first irreducible Brillouin zone: $k_1, k_2 \in [0, \frac{1}{2}]$. The term $e^{i\mathbf{K}\cdot\mathbf{x}}$ comes from the Bloch condition, which states that the solution is entirely periodic except for a phase shift across the unit cells' boundaries.

Based on Eq. (B9), we can obtain the following expression regarding the spatial derivative of the displacement function:

$$\frac{\partial^n}{\partial\mathbf{x}^n}[U(\mathbf{x}, t)] = (i^n)(\mathbf{K} + \mathbf{H})^n U(\mathbf{x}, t). \tag{B10}$$

Now, substituting the Fourier expansions of $A(\mathbf{x})$ and $I(\mathbf{x})$ [Eqs. (B4) and (B5)] into Euler-Bernoulli's governing equation for a two-dimensional structure yields

$$\frac{\partial^2}{\partial\mathbf{x}^2}\left[E\sum_{\mathbf{G}} \hat{I}(\mathbf{G})e^{i\mathbf{G}\cdot\mathbf{x}} \frac{\partial^2 U(\mathbf{x}, t)}{\partial\mathbf{x}^2}\right] + \rho\sum_{\mathbf{G}} \hat{A}(\mathbf{G})e^{i\mathbf{G}\cdot\mathbf{x}} \frac{\partial^2 U(\mathbf{x}, t)}{\partial t^2} = 0. \tag{B11}$$

Then, we further simplify this equation by applying the expressions in Eqs. (B9) and (B10):

$$\sum_{\mathbf{G}}\sum_{\mathbf{H}}[E(\mathbf{H}+\mathbf{K})^2(\mathbf{K}+\mathbf{H}+\mathbf{G})^2\hat{I}(\mathbf{G})-\omega^2\rho\hat{A}(\mathbf{G})] \times \hat{U}(\mathbf{H})e^{i(\mathbf{K}+\mathbf{G}+\mathbf{H})\cdot\mathbf{x}}=0. \tag{B12}$$

This leads to the characteristic equation of the corresponding eigenvalue problem

$$\sum_{\mathbf{G}}\sum_{\mathbf{H}}[E(\mathbf{H}+\mathbf{K})^2(\mathbf{K}+\mathbf{H}+\mathbf{G})^2\hat{I}(\mathbf{G})-\omega^2\rho\hat{A}(\mathbf{G})]=0. \tag{B13}$$

Since this characteristic equation must apply for all $\mathbf{G}$, we can select a specific $\mathbf{G}$ vector and solve the equation

$$\sum_{\mathbf{H}}[E(\mathbf{H}+\mathbf{K})^2(\mathbf{K}+\mathbf{H}+\mathbf{G})^2\hat{I}(\mathbf{G})-\omega^2\rho\hat{A}(\mathbf{G})]=0. \tag{B14}$$

The solution of this equation generates an eigenfrequency curve in the dispersion relationship.

Finally, we simplify the formulations above for the stretch-buckled kirigami sheet. Since the direct and reciprocal spaces of the stretched kirigami are both 1D periodic along the x direction, $\mathbf{x}=x\mathbf{e}_1$ and $\mathbf{G}=m_1\mathbf{b}_1$. Moreover, the orthogonality conditions from Eq. (B3) indicate that $\mathbf{e}_1\cdot\mathbf{b}_1=2\pi$. Substituting these expressions into Eqs. (B4) and (B5) yields the following two simplified equations for the Fourier expansion:

$$A(\mathbf{x})=\sum_{m_1}\hat{A}(m_1\mathbf{b}_1)e^{i(m_1\mathbf{b}_1\cdot\mathbf{x})}, \tag{B15}$$

$$I(\mathbf{x})=\sum_{m_1}\hat{I}(m_1\mathbf{b}_1)e^{i(m_1\mathbf{b}_1\cdot\mathbf{x})}, \tag{B16}$$

with the summation taken over all integers m_1.

To double check, let us increment the position vector by a period, $\mathbf{x}\to\mathbf{x}+a_1\mathbf{e}_1$, and validate that $A(\mathbf{x})$ and $I(\mathbf{x})$ do not change:

$$\begin{aligned}A(\mathbf{x}+a_1\mathbf{e}_1)&=\sum_{m_1}\hat{A}(m_1\mathbf{b}_1)e^{im_1\mathbf{b}_1\cdot(\mathbf{x}+a_1\mathbf{e}_1)}\\&=\sum_{m_1}\hat{A}(m_1\mathbf{b}_1)e^{im_1\mathbf{b}_1\cdot\mathbf{x}}e^{i2\pi a_1m_1}\\&=A(\mathbf{x}),\end{aligned} \tag{B17}$$

$$\begin{aligned}I(\mathbf{x}+a_1\mathbf{e}_1)&=\sum_{m_1}\hat{I}(m_1\mathbf{b}_1)e^{im_1\mathbf{b}_1\cdot(\mathbf{x}+a_1\mathbf{e}_1)}\\&=\sum_{m_1}\hat{I}(m_1\mathbf{b}_1)e^{im_1\mathbf{b}_1\cdot\mathbf{x}}e^{i2\pi a_1m_1}\\&=I(\mathbf{x}).\end{aligned} \tag{B18}$$

Note that $e^{i(2\pi a_1m_1)}$ equals one because a_1 and m_1 are integers. The origin of x is at the center of the unit cell. We can further simplify the Fourier expansion equations by plugging in $a_1=a$, where a as the unit cell's length, and $b_1=|\mathbf{b}_1|$ so that

$$\hat{A}(m_1\mathbf{b}_1)=\hat{A}(m_1)=\frac{1}{a}\int_{-a/2}^{a/2}A(x)e^{-i(2\pi m_1x)}dx, \tag{B19}$$

$$\hat{I}(m_1\mathbf{b}_1)=\hat{I}(m_1)=\frac{1}{a}\int_{-a/2}^{a/2}I(x)e^{-i(2\pi m_1x)}dx. \tag{B20}$$

Moreover, the 1D periodicity of kirigami indicates that $\mathbf{H}=n_1\mathbf{b}_1$, $\mathbf{K}=k_1\mathbf{b}_1$, and both $\mathbf{H}$ and $\mathbf{K}$ are along the x direction. Substituting the 1D simplifications of $\mathbf{H}$, $\mathbf{K}$, $\mathbf{G}$ into the Blotch theorem equation, Eq. (B9), will yield Eq. (2) in the main text. Furthermore, by substituting this 1D simplifications and Eqs. (B19) and (B20) into eigenvalue equation (B14), we eventually obtain the characteristic equation in 1D:

$$\sum_{n_1}\left[E(n_1+k_1)^2(k_1+n_1+m_1)^2\hat{I}(m_1)-\omega^2\left(\frac{\rho}{b_1^4}\right)\hat{A}(m_1)\right] =0. \tag{B21}$$

Solutions of this equation are summarized in Fig. 3(a).

APPENDIX C: COMSOL SIMULATION

Figure 6 details the meshed stretch-buckled kirigami sheet after the convergence study, using 3D solid elements. The mesh sizes are refined manually near the cut corners to ensure accurate simulation.

APPENDIX D: EXPERIMENTAL SETUP

Figure 7 details the complete experimental setup for measuring the transverse elastic wave transmissibility over the stretch-buckled kirigami sheet. It is worth noting that the unit cells in Fig. 3(b) appear different from each other, but this is an optical illusion. All unit cells in the kirigami prototype, except for the first and last ones at the boundary,

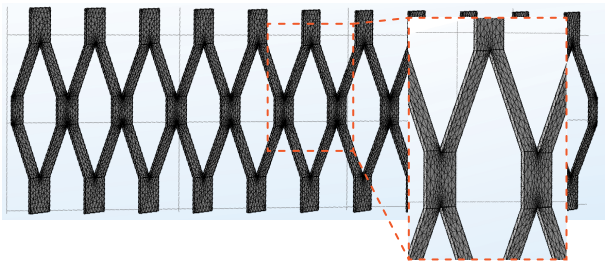

FIG. 6. Three-dimensional meshed model in COMSOL, showing the details near cut corners.

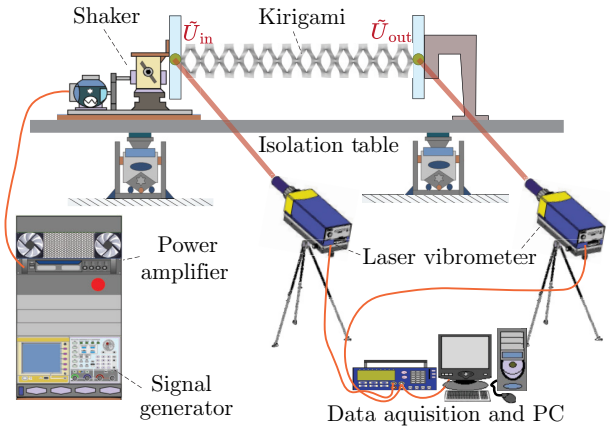

FIG. 7. A schematic diagram of the test apparatus.

have the same shape and dihedral angle. However, when the camera is placed in front of the kirigami prototype, every unit cell is at a slightly different angle with respect to the camera lens, so they appear different in the picture.

Moreover, we do not observe significant global plastic deformation in our stretched kirigami sample because the zig-zag distributed parallel cuts are intended to offer high stretchability and elastic response. Because of stress concentration, there are small and local plastic deformations at the tip of the slit cuts. These plastic deformations can be avoided by optimizing the cut tip shape, and they should not significantly affect the elastic wave band gaps at low frequency.

[1] Amir A. Zadpoor, Mechanical meta-materials, Mater. Horiz. **3**, 371 (2016).

[2] Katia Bertoldi, Vincenzo Vitelli, Johan Christensen, and Martin Van Hecke, Flexible mechanical metamaterials, Nat. Rev. Mater. **2**, 1 (2017).

[3] James Utama Surjadi, Libo Gao, Huifeng Du, Xiang Li, Xiang Xiong, Nicholas Xuanlai Fang, and Yang Lu, Mechanical metamaterials and their engineering applications, Adv. Eng. Mater. **21**, 1800864 (2019).

[4] Muamer Kadic, Graeme W. Milton, Martin van Hecke, and Martin Wegener, 3D metamaterials, Nat. Rev. Phys. **1**, 198 (2019).

[5] Jensen Li and Che Ting Chan, Double-negative acoustic metamaterial, Phys. Rev. E **70**, 055602 (2004).

[6] Farhad Javid, Pai Wang, Ali Shanian, and Katia Bertoldi, Architected materials with ultra-low porosity for vibration control, Adv. Mater. **28**, 5943 (2016).

[7] Fabrice Lemoult, Nadege Kaina, Mathias Fink, and Geoffroy Lerosey, Wave propagation control at the deep subwavelength scale in metamaterials, Nat. Phys. **9**, 55 (2013).

[8] Huanyang Chen and C. T. Chan, Acoustic cloaking in three dimensions using acoustic metamaterials, Appl. Phys. Lett. **91**, 183518 (2007).

[9] Hussein Nassar, Behrooz Yousefzadeh, Romain Fleury, Massimo Ruzzene, Andrea Alù, Chiara Daraio, Andrew N. Norris, Guoliang Huang, and Michael R. Haberman, Nonreciprocity in acoustic and elastic materials, Nat. Rev. Mater. **5**, 667 (2020).

[10] Farzad Zangeneh-Nejad, Dimitrios L. Sounas, Andrea Alù, and Romain Fleury, Analogue computing with metamaterials, Nat. Rev. Mater. **6**, 207 (2021).

[11] Manpreet Kaur, Tae Gwang Yun, Seung Min Han, Edwin L. Thomas, and Woo Soo Kim, 3D printed stretching-dominated micro-trusses, Mater. Des. **134**, 272 (2017).

[12] Brett G. Compton and Jennifer A. Lewis, 3D-printing of lightweight cellular composites, Adv. Mater. **26**, 5930 (2014).

[13] Li Yang, Ola Harrysson, Denis Cormier, Harvey West, Haijun Gong, and Brent Stucker, Additive manufacturing of metal cellular structures: Design and fabrication, Jom **67**, 608 (2015).

[14] R. C. Hayward, D. A. Saville, and Ilhan A. Aksay, Electrophoretic assembly of colloidal crystals with optically tunable micropatterns, Nature **404**, 56 (2000).

[15] Zhiguang Liu, Huifeng Du, Jiafang Li, Ling Lu, Zhi-Yuan Li, and Nicholas X. Fang, Nano-kirigami with giant optical chirality, Sci. Adv. **4**, eaat4436 (2018).

[16] Wenxia Hu, Zhiwen Ren, Zhishuai Wan, Dexing Qi, Xiaofei Cao, Zhen Li, Wenwang Wu, Ran Tao, and Ying Li, Deformation behavior and band gap switching function of 4D printed multi-stable metamaterials, Mater. Des. **200**, 109481 (2021).

[17] Sahab Babaee, Nicolas Viard, Pai Wang, Nicholas X. Fang, and Katia Bertoldi, Harnessing deformation to switch on and off the propagation of sound, Adv. Mater. **28**, 1631 (2016).

[18] Phanisri P. Pratapa, Phanish Suryanarayana, and Glaucio H. Paulino, Bloch wave framework for structures with nonlocal interactions: Application to the design of origami acoustic metamaterials, J. Mech. Phys. Solids **118**, 115 (2018).

[19] M Thota, S. Li, and K.W. Wang, Lattice reconfiguration and phononic band-gap adaptation via origami folding, Phys. Rev. B **95**, 064307 (2017).

[20] Zeming Song, Xu Wang, Cheng Lv, Yonghao An, Mengbing Liang, Teng Ma, David He, Ying-Jie Zheng, Shi-Qing Huang, and Hongyu Yu, *et al.*, Kirigami-based stretchable lithium-ion batteries, Sci. Rep. **5**, 1 (2015).

[21] Siheng Chen, Gary P. T. Choi, and L. Mahadevan, Deterministic and stochastic control of kirigami topology, Proc. Nat. Acad. Sci. **117**, 4511 (2020).

[22] Sahab Babaee, Simo Pajovic, Ahmad Rafsanjani, Yichao Shi, Katia Bertoldi, and Giovanni Traverso, Bioinspired kirigami metasurfaces as assistive shoe grips, Nat. Biomed. Eng. **4**, 778 (2020).

[23] Hesameddin Khosravi, Steven M. Iannucci, and Suyi Li, Pneumatic soft actuators with kirigami skins, Front. Robot. AI **8**, 749051 (2021).

[24] Yu-Chieh Cheng, Hao-Chuan Lu, Xuan Lee, Hao Zeng, and Arri Priimagi, Kirigami-based light-induced shape-morphing and locomotion, Adv. Mater. **32**, 1906233 (2020).

[25] Gary P. T. Choi, Levi H. Dudte, and L. Mahadevan, Programming shape using kirigami tessellations, Nat. Mater. **18**, 999 (2019).

[26] Shanshan Chen, Zhiguang Liu, Huifeng Du, Chengchun Tang, Chang-Yin Ji, Baogang Quan, Ruhao Pan, Lechen Yang, Xinhao Li, and Changzhi Gu, *et al.*, Electromechanically reconfigurable optical nano-kirigami, Nat. Commun. **12**, 1 (2021).

[27] Shanshan Chen, Jianfeng Chen, Xiangdong Zhang, Zhi-Yuan Li, and Jiafang Li, Kirigami/origami: Unfolding the new regime of advanced 3D microfabrication/nanofabrication with "folding", Light: Sci. Appl. **9**, 1 (2020).

[28] Doh-Gyu Hwang and Michael D. Bartlett, Tunable mechanical metamaterials through hybrid kirigami structures, Sci. Rep. **8**, 1 (2018).

[29] Yanbin Li, Qiuting Zhang, Yaoye Hong, and Jie Yin, 3D transformable modular kirigami based programmable metamaterials, Adv. Funct. Mater. **31**, 2105641 (2021).

[30] Amir Firouzeh and Jamie Paik, The design and modeling of a novel resistive stretch sensor with tunable sensitivity, IEEE Sens. J. **15**, 6390 (2015).

[31] Wei Zheng, Weicheng Huang, Feng Gao, Huihui Yang, Mingjin Dai, Guangbo Liu, Bin Yang, Jia Zhang, Yong Qing Fu, and Xiaoshuang Chen, *et al.*, Kirigami-inspired highly stretchable nanoscale devices using multidimensional deformation of monolayer mos2, Chem. Mater. **30**, 6063 (2018).

[32] Juhyeon Kim, Hyeji Park, and Soo-Hwan Jeong, A kirigami concept for transparent and stretchable nanofiber networks-based conductors and UV photodetectors, J. Ind. Eng. Chem. **82**, 144 (2020).

[33] Yichao Tang and Jie Yin, Design of cut unit geometry in hierarchical kirigami-based auxetic metamaterials for high stretchability and compressibility, Extreme Mech. Lett. **12**, 77 (2017).

[34] Ahmad Rafsanjani and Katia Bertoldi, Buckling-Induced Kirigami, Phys. Rev. Lett. **118**, 084301 (2017).

[35] Midori Isobe and Ko Okumura, Initial rigid response and softening transition of highly stretchable kirigami sheet materials, Sci. Rep. **6**, 1 (2016).

[36] Aditya Lele, Vishrut Deshpande, Oliver Myers, and Suyi Li, Snap-through and stiffness adaptation of a multi-stable kirigami composite module, Compos. Sci. Technol. **182**, 107750 (2019).

[37] Hang Zhang, Jun Wu, and Daining Fang, and Yihui Zhang, Hierarchical mechanical metamaterials built with scalable tristable elements for ternary logic operation and amplitude modulation, Sci. Adv. **7**, eabf1966 (2021).

[38] G. Trainiti, J. J. Rimoli, and M. Ruzzene, Wave propagation in periodically undulated beams and plates, Int. J. Solids Struct. **75-76**, 260 (2015).